COMMUNICATION

DOI: 10.1039/x0xx00000x

Functionalized boron nanosheets as an intelligent nanoplatform for synergistic low-temperature photothermal therapy and chemotherapy

Zi Fu,[a] Gareth R. Williams,[b] Shiwei Niu,[a] Jianrong Wu,[*c] Feng Gao,[d] Xuejing Zhang,[a] Yanbo Yang,[a] Yu Li,[a] and Li-Min Zhu[*a]

2D nanomaterials have attracted special attention in biomedicine, owing to their surface effect and fascinating quantum size. In this work, an innovative boron-based multifunctional nanoplatform was developed for synergistic chemotherapy/low temperature photothermal therapy (PTT). The platform is functionalized with the cRGD peptide to permit tumor targeting toward $\alpha_v\beta_3$ integrin over-expressed cells. The nanoparticles were further loaded with the chemotherapeutic doxorubicin (DOX) and a heat shock protein inhibitor (17AAG), and the loading capacity of DOX (60.3%) and 17AAG (41.7%) (w/w) was obtained, respectively. The resultant DOX-17AAG@B-PEG-cRGD system shows both pH-controlled and near-infrared (NIR)-induced DOX and 17AAG release. It also gives significantly enhanced cellular uptake in cancerous cells over healthy cells. The presence of 17AAG permits low-temperature PTT to be combined with chemotherapy from DOX, resulting in highly effective anti-cancer activity. This has been confirmed by both *in vitro* assays and using an *in vivo* murine cancer model. It is expected that such multifunctional nanoplatform can serve as a promising candidate for cancer therapy.

1 Introduction

Cancer is a disease that seriously endangers human health.[1] Traditional chemotherapeutic drugs have limited clinical applications due to their low specificity, which results in inevitable off-target toxicity, and because they typically have low water solubility and bioavailability. In order to solve these problems, custom-designed drug delivery systems (DDSs) have been developed to target delivery of an active pharmaceutical ingredient (API) to tumor sites.[2-5] The accumulation of APIs at the tumor can be enhanced by both passive (enhanced permeability and retention effect, EPR) and active targeting methods.[6] In recent years, therapeutic nanoscale systems based on inorganic materials have attracted extensive research interest in cancer therapy. If well-designed, such formulations can have excellent biocompatibility and pharmacokinetic profiles, effective active/passive targeting and significant therapeutic effects.[7,8] Two-dimensional (2D) nanomaterials in particular have been explored for potential applications in drug delivery, photothermal therapy, diagnosis, biosensing, and tissue engineering.[9-11] A wide range of 2D materials exist, including transition metal disulfides, carbides, oxides, nitrides or carbonitrides, graphene, or black phosphorus.[8,12-17]

Although a variety of 2D nanomaterials have been reported, the research on single-element boron is still rare. In recent years, boron sheet has received extensive attention due to its excellent physical and chemical properties (e.g., superconductivity, exceptional structural complexity, and efficient photothermal conversion efficiency). Boron-based systems have been found to possess excellent biocompatibility and high chemical stability, indicating their great potential for application in the biomedical field.[18-21] It has been proved that boron nanosheets (NSs) have potential in photothermal therapy (PTT) and drug delivery.[21] Unfortunately, the clinical translation of inorganic DDSs is hampered by their having short blood circulation times and undergoing rapid clearance by the RES (reticuloendothelial system).[22] To enhance the biocompatibility and improve its sensitivity and specificity, surface modification approaches are often employed.[23] Polyethylene glycol (PEG) is the most common surface functionalization moiety. Coating with PEG leads to reduced nonspecific protein adsorption and immunogenicity, which allow for extended circulation times and for DDSs to accumulate at a tumor site.[24-26] Tumor-specific targeting ligands (e.g. RGD, arginine-glycine-aspartic acid) have also been applied to enhance the preferential accumulation of DDSs in tumors, which arises owing to the peptides' high affinity with over-

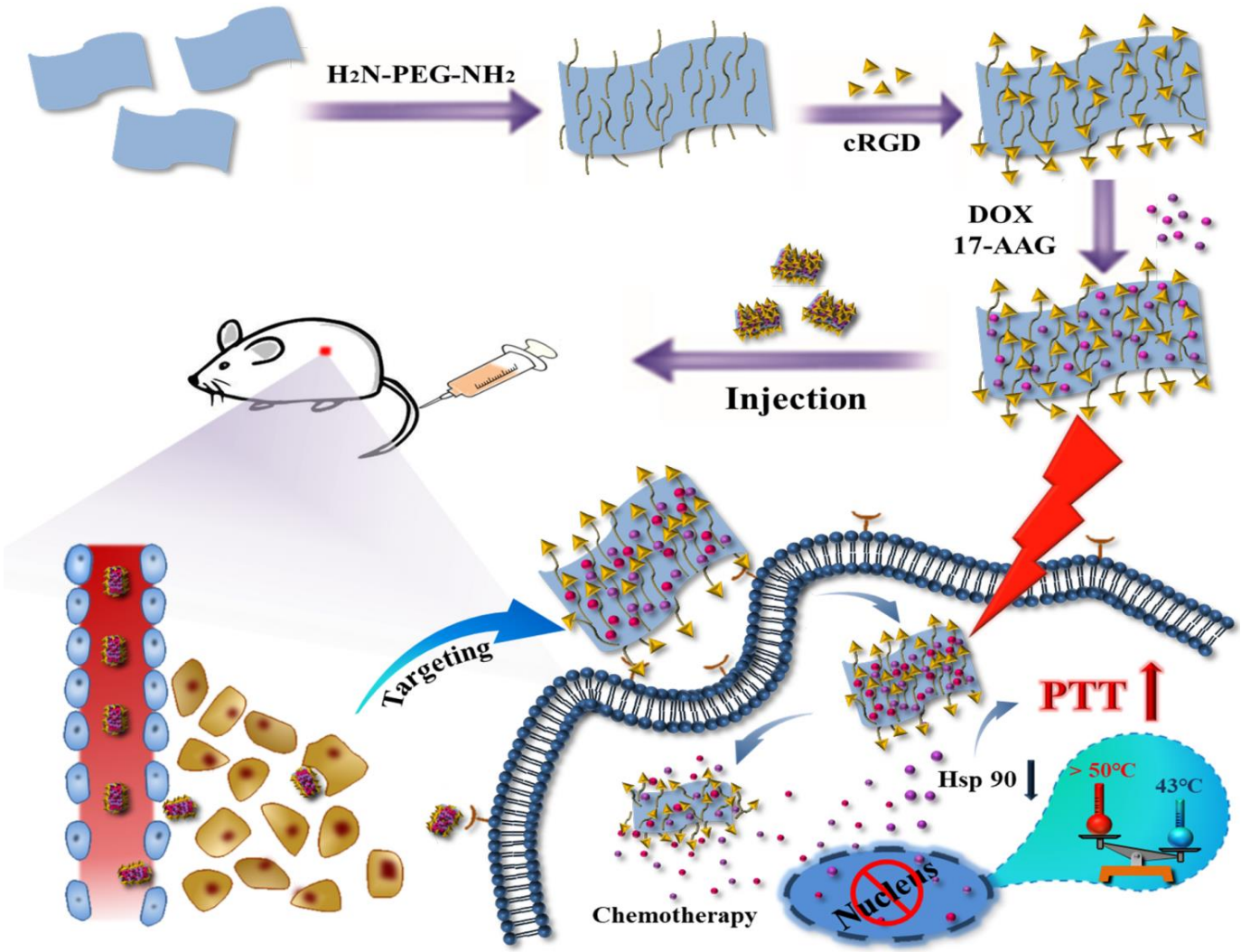

Fig.1. A schematic illustration of the synthetic approach used in this work.

expression of receptors on cancer cells.[27,28]

PTT is a novel cancer treatment method which can be used to inhibit tumor growth with high efficiency.[8,13,16] Compared with traditional cancer treatments such as chemotherapy, surgery and radiation therapy, PTT is advantageous because it is minimally invasive, with reduced side effects and higher therapeutic efficacy.[29] Combinations of PTT and chemotherapy are particularly potent for tumor inhibition.[7,30]

However, a concern in the application of PTT is the risk of increasing cancer cells' tolerance of heat stress, which could decrease efficacy and cause tumor recurrence.[31-33] To ensure therapeutic efficacy, local temperatures of >50 °C are often needed.[34] However, healthy organs and tissues near the tumor may be damaged by such high temperatures.[31,35] Therefore, reducing the heat-resistance response of cancer cells to maximize the PTT effect is a potential strategy. To ameliorate this issue, low-temperature PTT strategies have been proposed and resulted in excellent anti-cancer effects.[36-39]

Heat shock proteins (HSPs) play a crucial role in protecting an organism exposed to hyperthermia, and thus inhibiting expression of these is one route by which low temperature PTT can be implemented.[40,41] According to the previous study, HSP90 inhibitor 17AAG (allylamino-17-demethoxygeldanamycin) can effectively target HSP90 to reduce the heat resistance, thereby achieving effective tumor suppression and ablation.[39] Our group recently developed a biodegradable organosilica-based formulation loaded both with a photothermal agent and heat-shock protein inhibitor. This was found to inhibit cancer cell replication, promote tumor ablation, and minimize side effects through the use of low temperature conditions.[36] This combination of chemotherapy, HSP inhibitors and PTT agents appears to be powerful, but to date such a synergistic system has not been explored with B nanosheets carriers.

In this work, we designed and synthesized a boron-based multifunctional nanoplatform co-carrying doxorubicin (DOX) and the heat shock protein inhibitor 17AAG, which can kill cancer cells and inhibit tumor growth at relatively low temperature (Fig. 1). B nanosheets were first prepared by a top-down method, and then surface modified with both H_2N-PEG-NH_2 and cRGD by electrostatic adsorption and amide reaction, respectively. This functionalization should both extend their half-life in vivo and also mediate specific tumor targeting. The resultant B-PEG-cRGD NSs were characterized and the photothermal performance was evaluated. Next, DOX and 17AAG were co-loaded onto the B-PEG-

cRGD nanosheets. The potential of the DOX-17AAG@B-PEG-cRGD nanosheets for synergistic low-temperature PTT and chemotherapy was evaluated both *in vitro* and *in vivo*.

2 Results and discussion

2.1 Synthesis and characterization of DOX-17AAG@B-PEG-cRGD

Boron nanosheets (B NSs) were obtained by a top-down method following a previously reported protocol.[21] The sheet morphology was first investigated by transmission electron microscopy (TEM) and atomic force microscopy (AFM). The B NSs exhibit irregularly shaped sheet structures (Fig. 2a). AFM image revealed that the boron nanosheets have a thickness of about 6.1 nm, which corresponds to a single layer (Fig. 2b, c). Fig. 2d depicts X-ray photoelectron spectroscopy (XPS) data. As well as exhibiting peaks from B, the XPS spectrum indicates the presence of O in the nanosheets. This is due to the formation of boron oxide during the thermal oxidation etching process. As shown in Fig. 2e, there are peaks in the B 1s region consistent with two different B-B bonds, as well as B-O bonds, which also explains the negative zeta potential (-26.3 mV) detected (Fig. S1, Supporting Information).

Having verified the successful synthesis of the B nanosheets, these were then subjected to surface modification. First, the B NSs were modificated with H_2N-PEG-NH_2 via electrostatic adsorption to obtain PEGylated B NSs (B-PEG), which improve their biocompatibility and dispersion stability. The zeta potential was observed to become less negative after the introduction of H_2N-PEG-NH_2 groups (Fig. S1), demonstrating successful surface coating.

Under weakly acidic conditions, the amine groups of B-PEG were then reacted with the carboxyl group of the polypeptide cRGD, to form B-PEG-cRGD. Zeta potential measurements of each grafting step (Fig. S1) revealed that the potential of B-PEG-cRGD rise to −12.4 ± 0.76 mV after the addition of cRGD. This is due to cRGD being overall positively charged under weakly acidic conditions. Furthermore, the hydrodynamic diameter of B-PEG-cRGD increased to ca. 157 nm, compared to B nanosheets with a mean diameter of about 136 nm (Fig. S2). Thermogravimetric analysis (TGA, Fig. S3) indicates that the content of H_2N-PEG-NH_2 and cRGD in the B-PEG-cRGD system is 1.6% and 1.3% (w/w), respectively. When the B-PEG-cRDG particles are suspended in phosphate buffered saline, their size is observed to remain constant over 24 h, in contrast to the B NSs which exhibit a gradual increase in size indicating aggregation (Fig. S4).

The B-PEG-cRGD nanosheets were next loaded with DOX and 17AAG via physical adsorption.[38] UV-vis spectra (Fig. 2f) show DOX to have characteristic absorption peaks at 480 nm and 200–250 nm; these can also be seen in the spectrum of DOX–17AAG@B-PEG-cRGD. There is also an additional peak at 340 nm in the DOX–17AAG@B-PEG-cRGD spectrum, which corresponds to the presence of 17AAG. Drug loading is critical to assess its therapeutic efficacy against a potential drug delivery system. Based on the optimized feed ratio, the loading capacity of DOX (60.3%) and 17AAG (41.7%) (w/w) was calculated from UV and HPLC data, respectively (Fig. S5 and S6). After DOX loading, the zeta potential rises to +23.7 ± 1.17 mV (due to the presence of

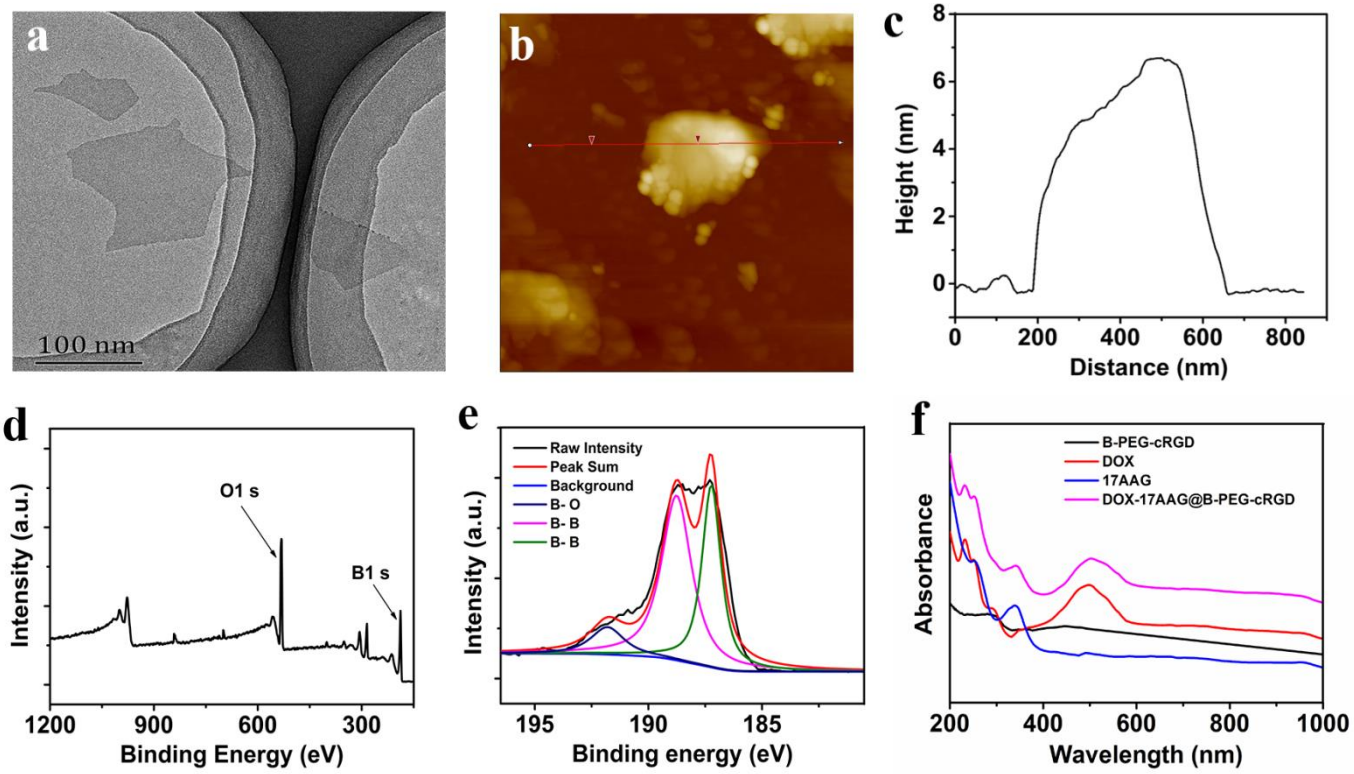

Fig.2. (a) TEM image of B NSs; (b) AFM image and (c) thickness of B NSs; (d) XPS survey spectrum of B NSs; (e) An enlargement of the B 1s region in XPS; (f) UV–vis absorption spectra of different nanoparticles.

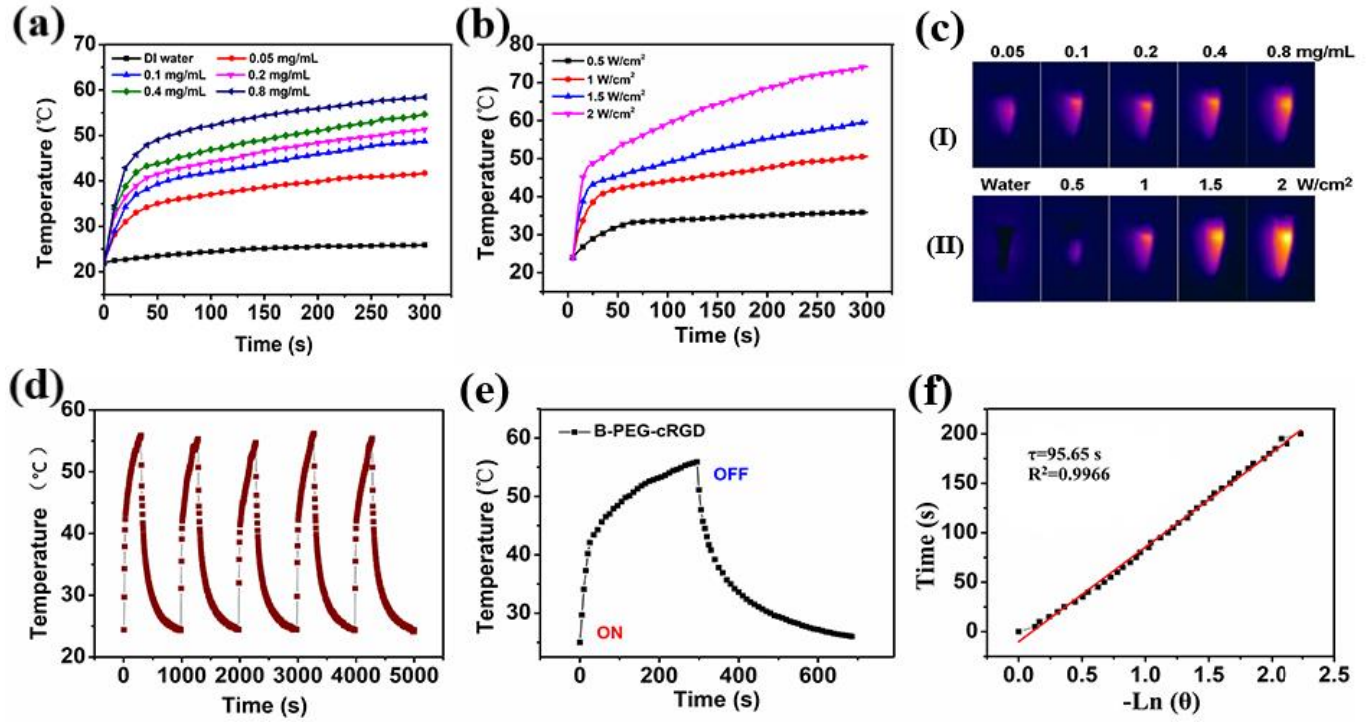

Fig.3. PTT data (a) Temperature variation curves of B-PEG-cRGD suspensions at different concentrations with a laser power density of 1 W/cm^2. (b) Temperature variation curves of 0.2 mg/mL suspensions at different laser power densities. (c) Photothermal images of B-PEG-cRGD suspensions (I) at different concentrations and 1 W/cm^2 laser power and (II) at 0.2 mg/mL and exposed to different power 808 nm laser irradiation. (d) Temperature changes for a B-PEG-cRGD suspension (0.8 mg/mL) irradiated at 2 W/cm^2 over five on–off cycles. (e) Photothermal activity of B-PEG-cRGD (0.2 mg/mL) with laser irradiation (1.5 W/cm^2) for 5 min, showing the cooling period. (f) The linear regression between cooling time and –ln θ.

amine groups in DOX) and then after 17AAG is added the potential declines to -27.4 ± 0.4 mV.[36] The serial changes of zeta potential evidence the successful formation of DOX-17AAG@B-PEG-cRGD.

2.2 Photothermal effects

The photothermal properties and photostability of the nanomaterials were evaluated under exposure to an 808 nm NIR laser. The temperature of suspensions of B-PEG-cRGD increased with their concentration (Fig. 3a). After 5 min of NIR laser irradiation at 1 W/cm^2, the temperature of a 1 mg/mL suspension reached 58.5 °C (Fig. 3a), which will cause irreversible damage to tumor cells. In contrast, the temperature of pure water increased by only 2.7 °C under the same conditions. Greater increases in the temperature of the suspension were observed as the power density was increased (Fig. 3b). Photothermal images (Fig. 3c) confirm concentration and power-dependent temperature increases. The above data all show the B-PEG-cRGD NSs to be potent PTT agents. The B-PEG-cRGD NSs are observed to have stable PTT properties over 5 on/off cycle of laser irradiation (Fig. 3d). Photothermal conversion efficiency (PTCE) of the B-PEG-cRGD NSs was calculated following methods used in previous reports (see Fig. 3e and 3f), and determined to be 41%. This is similar to that previously reported for B NSs-based compounds，and higher than other inorganic-based PTAs such as graphene oxide (25%) and black phosphorus analogue compounds (39.3%).[21,42,43]

2.3 Drug release

Stimuli-responsive drug delivery systems have received much attention because of their ability to target the tumor site.[44] The B-PEG-cRGD NSs are expected to respond to changes in pH and also to NIR irradiation.[43,44] Hence, DOX and 17AAG release was investigated at two different pH values (pH=5.0 or 7.4), with or without laser irradiation. The results are given in Fig. 4a, b. At the physiological pH (7.4) and without NIR exposure, the cumulative release of DOX reached approximately 17.7% after 24 h (Fig. 4a), much lower than at pH 5.0 (40.4%), indicating the formulation's pH responsive characteristics. These can be attributed to the protonation of DOX under acidic conditions, which increases its solubility and encourages release. Under NIR laser stimulation, the release of DOX is further promoted, reaching 64.0% after 24 h at pH 5.0 with NIR irradiation. This is because the local heating caused by the laser reduces the strength of interactions between the NSs and DOX. Similar release behavior was seen for 17AAG (Fig. 4b).

2.4 *In vitro* cellular uptake

The ability of the DOX-17AAG@B-PEG-cRGD nanocomplex to target cancer cells was evaluated in MDA-MB-231 (cancerous) and HUVEC (healthy) cells using confocal laser scanning microscopy (CLSM). The resultant images (Fig. 4c) revealed that both cell lines showed a certain amount of free DOX uptake. In addition, it is observed that the fluorescence intensity of DOX in MDA-MB-231 cells treated with

DOX-17AAG@B-PEG-cRGD is higher than that of HUVEC cells, due to the overexpression of integrins ($\alpha_v\beta_3$ and $\alpha_v\beta_5$) on MDA-MB-231 cells and the ability of the cRGD sequences on the surface of the nanocomposites to be specifically recognized by these.[45]

Afterward, the cellular uptake of DOX-17AAG@B-PEG-cRGD nanocomposites was further quantitatively studied by flow cytometry. As shown in Fig. 4d, the DOX fluorescence intensity of the DOX-17AAG@B-PEG-cRGD group is much higher than free DOX group, which indicates that DOX-17AAG@B-PEG-cRGD can be specifically recognized by MDA-MB-231 cells. The above data demonstrate active targeting of the nanocomposites to MDA-MB-231 cells.

2.5 *In vitro* cytotoxicity

The cytotoxicity of the carrier B NSs and B-PEG-cRGD NSs was evaluated in vitro with the CCK-8 assay. Cells treated with the nanomaterials have high viabilities, above 90% even at a concentration of 300 μg/mL (Fig. S7). In addition, we studied the toxicity of NIR-mediated B-PEG NSs in MDA-MB-231 cells. As shown in the Fig. S8, cell cytotoxicity is highly concentration-dependent. The treatment by B-PEG NSs under laser irradiation at a

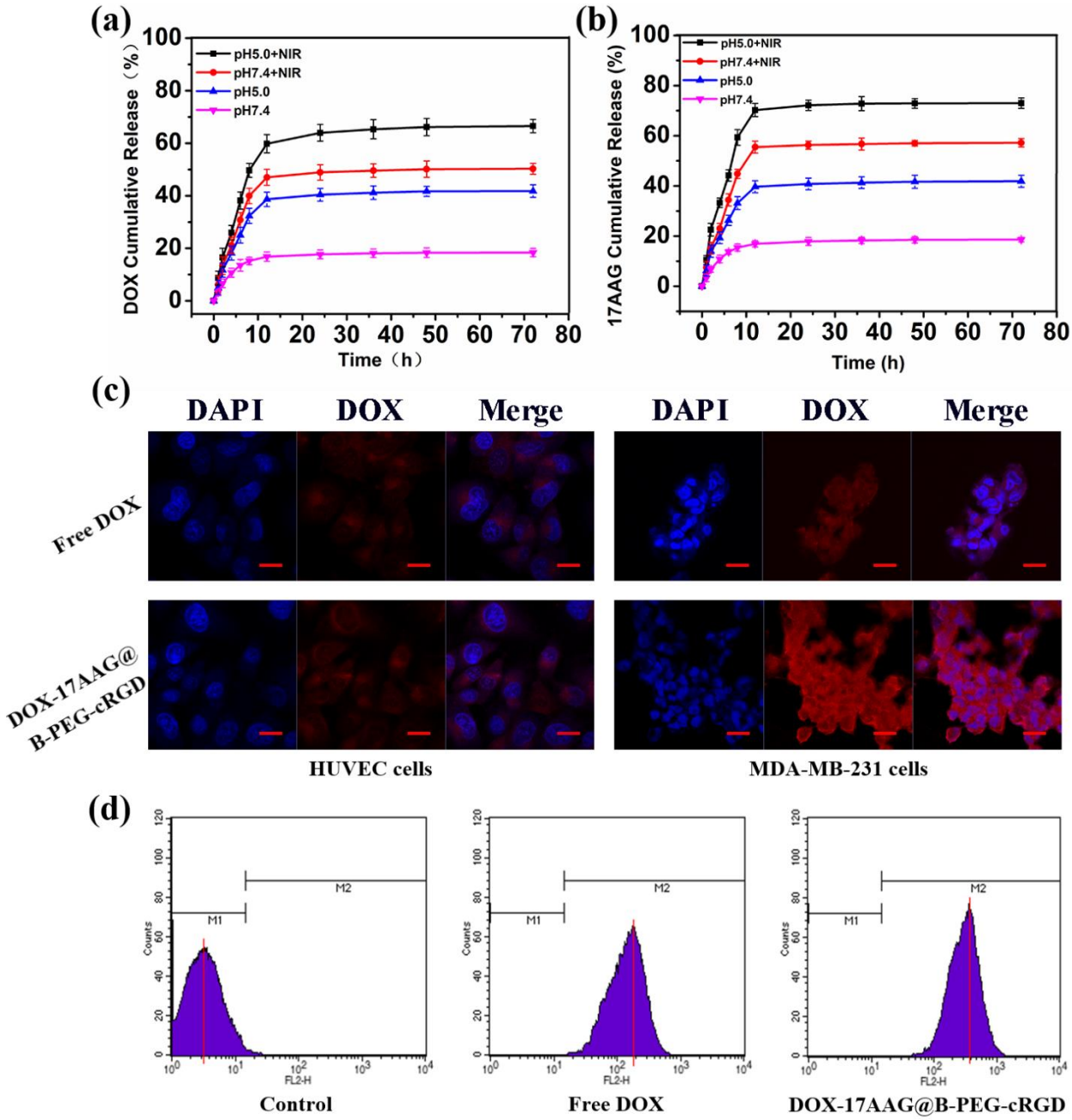

Fig.4. *In vitro* (a) DOX and (b) 17AAG release from DOX-17AAG@B-PEG-cRGD (mean ± S.D.; n = 3). (c) Confocal fluorescence images of HUVEC and MDA-MB-231 cells treated with free DOX or DOX-17AAG@B-PEG-cRGD (scale bar: 50 μm). (d) Flow cytometry data of MDA-MB-231 cells incubated with PBS (control), free DOX, and DOX-17AAG@B-PEG-cRGD.

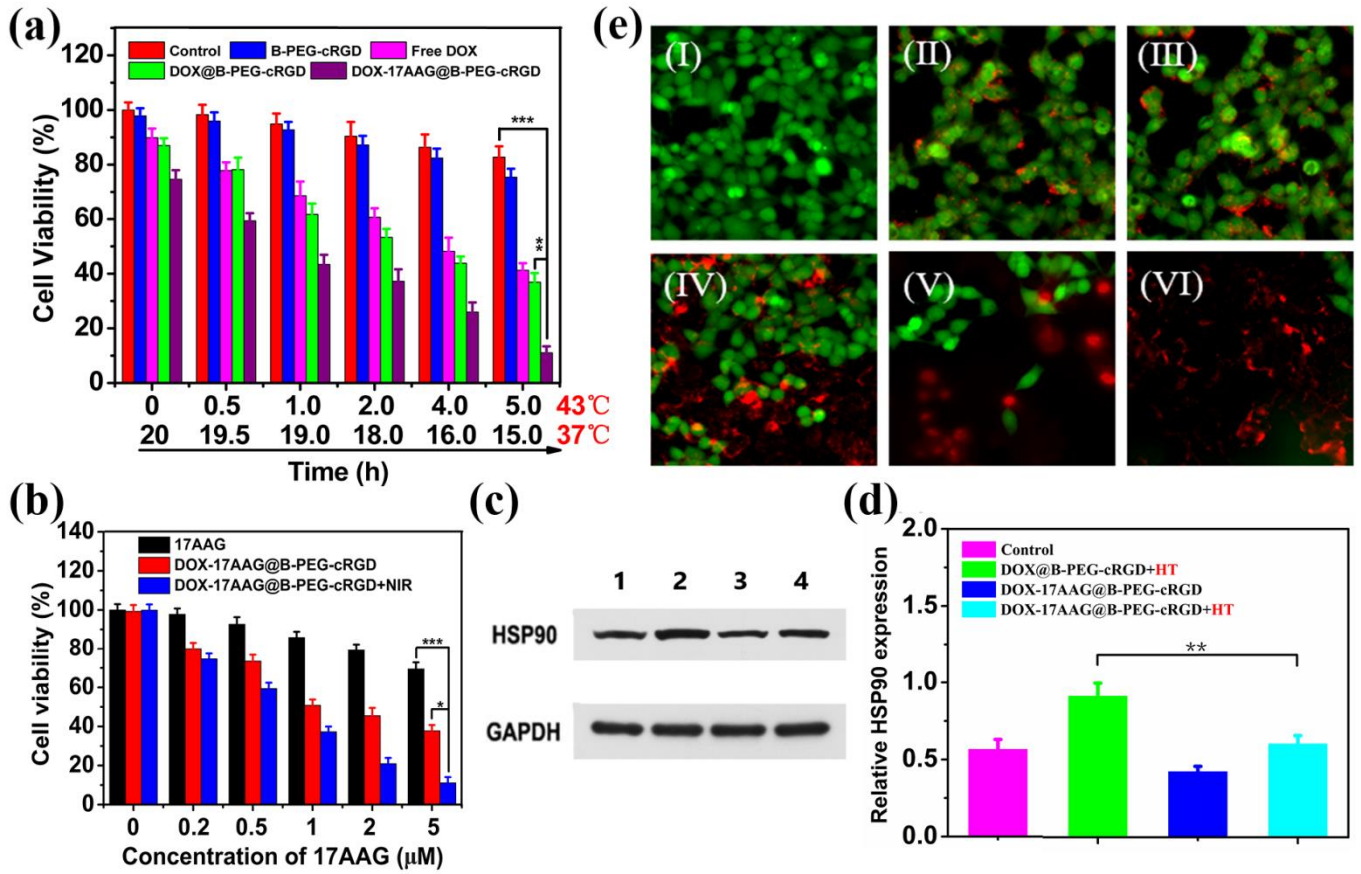

Fig.5. (a) Relative cell viabilities of MDA-MB-231 cells initially incubated at 43 °C and then at physiological temperature (37 °C). (b) Relative viabilities of MDA-MB-231 cells after incubation with different formulations at various 17AAG concentrations, with or without laser irradiation (808 nm, 0.5 W/cm^2, 20 min). (c) Western blotting analysis and (d) quantified Hsp90 expression levels in MDA-MB-231 cells after treatment for 4 h. (e) Fluorescence images of MDA-MB-231 cells costained with calcein AM/PI after different treatments. (I) Control; (II) B-PEG-cRGD+NIR; (III) free DOX; (IV) DOX-17AAG@B-PEG; (V) DOX@B-PEG-cRGD+NIR; (VI) DOX-17AAG@B-PEG-cRGD+NIR.

concentration of 200 μg/mL resulted in more than 80% of cells being effectively killed. The carrier materials therefore have high cytocompatibility. Next, we investigated the effect of low-temperature hyperthermia on cancerous cells. It was hypothesised that the presence of 17AAG would inhibit the expression of Hsp90, reducing the heat tolerance of tumor cells. To explore this, MDA-MB-231 cells were cultured with B-PEG-cRGD, free DOX, DOX@B-PEG-cRGD or DOX-17AAG@B-PEG-cRGD. The cells were cultured for a total of 20 h. Initially they were incubated at 43 °C, before being transferred to 37 °C for the remainder of the experimental period. The DOX-17AAG@B-PEG-cRGD particles were toxic to tumor cells at both temperatures, as depicted in Fig 5a. It was observed that the cells have much lower cell viabilities after treatment with 17AAG and DOX-17AAG@B-PEG-cRGD and low-temperature hyperthermia at 43 °C for 5 h. The cell viability of the DOX@B-PEG-cRGD group was significantly higher than that of the DOX-17AAG@B-PEG-cRGD group under these conditions, which can be attributed to the presence of 17AAG inhibiting heat shock protein expression and thus preventing the cells from deploying their protective mechanisms to hyperthermia.

The cytotoxic properties of the DOX-17AAG@B-PEG-cRGD systems were next explored at a range of equivalent 17AAG concentrations (Fig. 5b). The results show that 17AAG gives concentration-dependent inhibition of cell growth. However, cells treated with free 17AAG still have relatively high viability even at a concentration of 5 μM.[46,47] It was seen that cells treated with DOX-17AAG@B-PEG-cRGD and NIR irradiation showed significantly more death compared to those given free 17AAG or DOX-17AAG@B-PEG-cRGD without laser irradiation. This is primarily owing to the synergy provided by a low-temperature PTT/chemotherapy combined treatment.

To verify the effect of 17AAG on the ability of cells to withstand heat, we studied the expression of Hsp90 in MDA-MB-231 cells by western blot analysis, with glyceraldehyde-3-phosphate dehydrogenase (GAPDH) as a control (Fig. 5c, d). The expression of Hsp90 in cells exposed to DOX@B-PEG-cRGD was up-regulated after a heat treatment. However, the expression of Hsp90 was significantly inhibited after treatment with the 17AAG-loaded nanocomplex, which demonstrates that 17AAG can down-regulate the expression of Hsp90, thus rendering cells more vulnerable to heat.

A calcein-AM/PI double staining assay was conducted to visually assess the cells after the different treatments (Fig. 5e). Cells treated with DOX-17AAG@B−PEG-cRGD under NIR laser irradiation

illustrated the highest extent of cell death (red fluorescence). Together, these results indicate that low-temperature PTT/chemotherapy synergistic therapy showed significantly greater therapeutic effects than a single therapy. Clearly, treatment with DOX-17AAG@B–PEG-cRGD under laser irradiation can provide targeted drug delivery and synergistic anticancer therapy in vitro.

2.6 *In vivo* biodistribution

Next, we studied the biodistribution and accumulation of DOX-17AAG@B-PEG-cRGD in vivo through inductively coupled plasma optical emission spectrometer (ICP-OES) spectroscopic analysis. After 8 h intravenous injection, DOX-17AAG@B-PEG-cRGD could efficiently accumulate into tumor tissues with a targeting efficacy of 12.3%, which was significantly higher than that of DOX-17AAG@B-PEG group (6.4%), as revealed in Fig. 6a. The efficient active targeting of cRGD modified nanosheets was expected to facilitate and enhance its high therapeutic efficacy in vivo on tumor xenograft. In addition, we collected the feces and urine from mice after DOX-17AAG@B-PEG-cRGD treatment to evaluate the in vivo metabolism of DOX-17AAG@B-PEG-cRGD nanocomposite. After 8 h intravenous administration, feces and urine both showed the maximum B content, and then gradually decreased with time (Fig. 6b). The results indicate that the DOX-17AAG@B-PEG-cRGD nanocomposites can be effectively eliminated by means of feces and urine.

2.7 *In vivo* therapeutic efficacy

The anticancer potential of DOX-17AAG@B-PEG-cRGD in vivo was additionally evaluated. Nude mice bearing MDA-MB-231 tumors were randomly divided into six groups (n= 5 per group) as follows: group 1: PBS (control), group 2: B-PEG-cRGD+NIR, group 3: free DOX, group 4: DOX-17AAG@B-PEG, group 5: DOX@B-PEG-cRGD+NIR, group 6: DOX-17AAG@B-PEG-cRGD+NIR. The mice in groups 1, 5, and 6 were irradiated under an 808 nm NIR laser with a power density of 1 W/cm^2 for 5 min after injection, and in vivo thermal images were recorded using an IR infrared camera. Under the same laser irradiation, the tumor temperature of mice treated with DOX@B-PEG-cRGD or DOX-17AAG@B-PEG-cRGD both rapidly increased by about 16 °C to over 43 °C, whereas the tumors temperature of mice given a PBS treatment showed negligible changes (Fig. 6c, d). The tumor size was monitored over 14 days (see Fig. 7a). Tumor growth was most notably inhibited by DOX-17AAG@B-PEG-cRGD in combination with NIR laser irradiation, with no increase in tumor volume noted throughout the treatments experimental period (Fig. 7a, b). DOX@B-PEG-cRGD+NIR treatment led to a slower rate of increase in the tumor volume than was observed with the control animals, but growth is still evident. It is worth nothing that no obvious weight changes were seen with any of the treatments except the free DOX group, which confirmed the nanoplatform to have good biocompatibility (Fig. 7c). Free DOX, in contrast, results in a decline in body weight with time, owing to its off-target toxicity. Survival curves showed that mice treated with DOX-17AAG@B-PEG-cRGD+NIR had longer survival times than the other groups, and no mouse death occurred during the observation period (Fig. 7d).

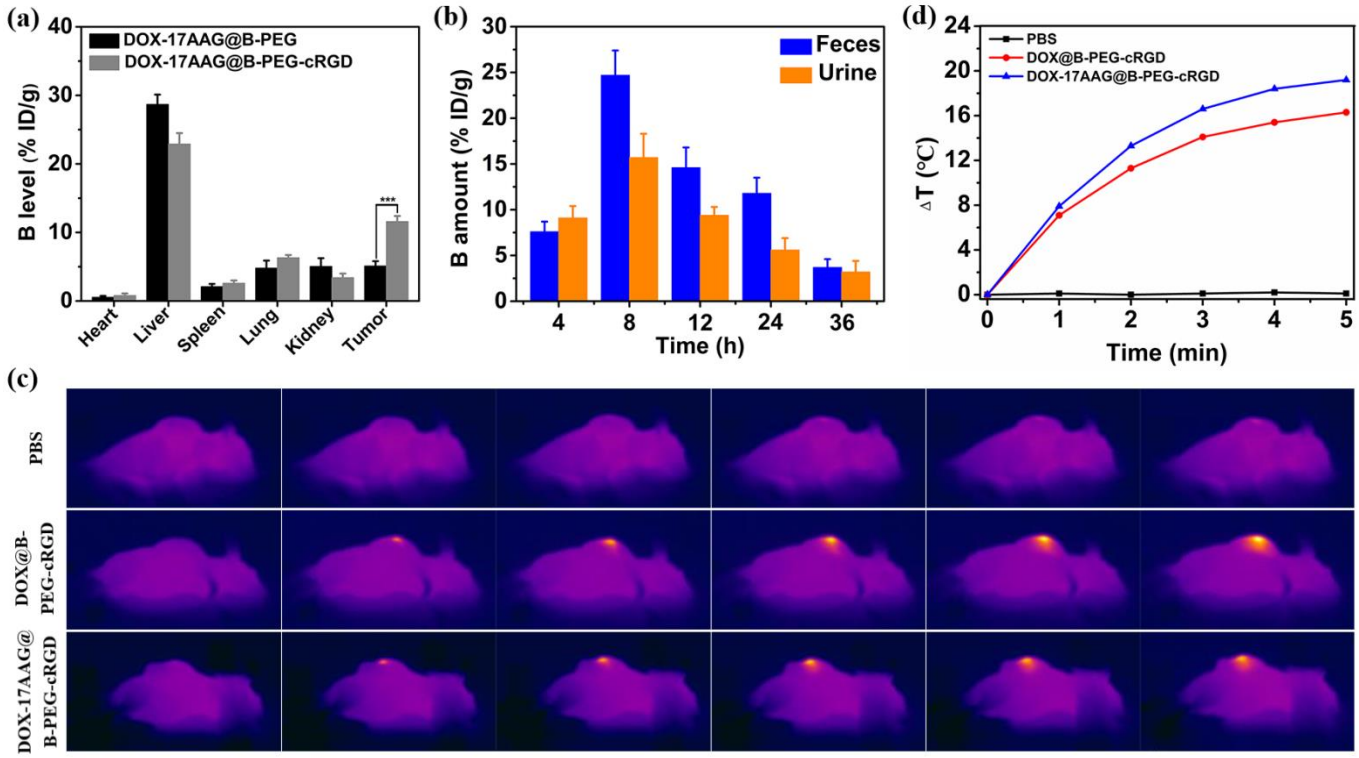

Fig. 6. (a) *In vivo* biodistribution of B (% ID of per gram of tissues) in main tissues and tumor after treatment with DOX-17AAG@B-PEG and DOX-17AAG@B-PEG-cRGD for varied time intervals. (b) Time-dependent B content changes in feces and urine after administration of DOX-17AAG@B-PEG-cRGD. (c) Thermal images and (d) the corresponding temperature changes of MDA-MB-231 tumor-bearing mice after different treatments.

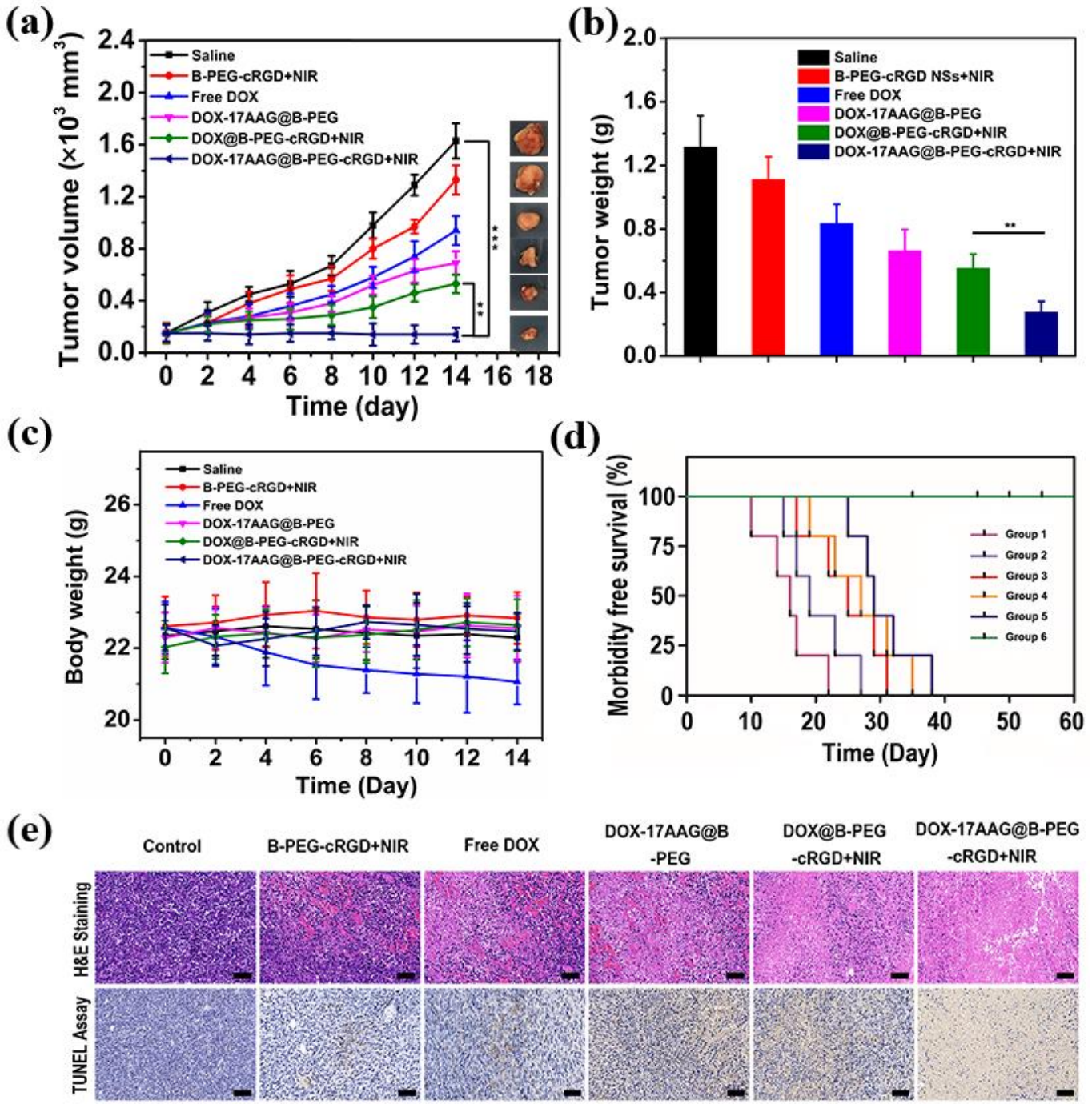

Fig. 7. (a) Tumor growth curves and representative images. (b) The tumor masses after 14 days of treatment. (c) Body weight changes with time. (d) Morbidity free survival curves. Group 1: saline; Group 2: B-PEG-cRGD + NIR; Group 3: Free DOX; Group 4: DOX-17AAG@B-PEG; Group 5: DOX@B-PEG-cRGD + NIR; Group 6: DOX-17AAG@B-PEG-cRGD + NIR. (e) Images of H&E (top) and TUNEL (bottom) stained tumor tissues slices (scale bar: 50 μm).

2.8 Histological analysis

After the end of the treatment period, the major organs and tumors of the mice were excised and hematoxylin and eosin (H&E) and TUNEL staining applied (Fig. 7e). The HE staining results showed that compared with the control group and other treatment groups, the DOX-17AAG@B-PEG-cRGD+NIR group caused more tumor cell apoptosis. Large areas of necrotic and apoptotic cells in the tumor area (brown dots) can be observed for the synergistic treatment group in TUNEL staining.

To probe for any potential toxicity, the heart, liver, spleen, lung, and kidney tissues of mice treated with DOX-17AAG@B-PEG-cRGD+NIR, were analysed by H&E staining (Fig. S9). It can be seen from the images that there was no obvious inflammation, organ damage, or any other pathological changes in the treatment group. The nanocomplex therefore has good biocompatibility in vivo.

3 Conclusion

A multifunctional nanoplatform based on boron nanosheets was developed in this work for synergistic low-temperature photothermal therapy (PTT)/chemotherapy of cancer. This formulation exhibits high photothermal conversion efficiency (41.3%) and could be loaded with doxorubicin (DOX, a chemotherapeutic) and the heat shock protein inhibitor 17AAG to yield the multifunctional DOX-17AAG@B-PEG-cRGD system. DOX and 17AAG release are accelerated by exposure to NIR light and acidic pH. The presence of cRGD in the system endows DOX-17AAG@B-PEG-cRGD with active tumor-targeting capabilities, as was demonstrated by in vitro uptake experiments. The inclusion of 17AAG reduces the ability of cancer cells to withstand heat, and DOX-17AAG@B-PEG-cRGD hence effectively induces apoptosis of cancer cells at relatively low temperatures. In vitro and in vivo experiments demonstrated that the DOX-17AAG@B-PEG-cRGD nanoplatform can effectively kill cancer cells and completely inhibit tumor growth, which is attributed to the combination of low temperature PTT and chemotherapeutic outcomes. The DOX-17AAG@B-PEG-cRGD is hence has significant potential for advanced, targeted, anticancer therapeutics.

4 Methods and experimental

4.1 Materials

Boron powder, doxorubicin (DOX), N-methyl-2-pyrrolidone (NMP), ethanol, N-[3-(dimethylamino)propyl]-N′-ethyl-carbodiimide hydrochloride (EDC), dimethyl sulfoxide (DMSO), and phosphate buffered saline (PBS) were ordered from Aladdin Industrial Inc. (Shanghai, China). H_2N-PEG-NH_2 (*Mw* = 2000) was provided by Yare Biotech, Inc. (Shanghai, China). Tanespimycin (17-AAG) was purchased from Dalian Meilun Biotech Co., Ltd. (Dalian, China). RGD peptide was supplied by Spec-Chem Industry Inc. (Nanjing, China). A Cell Counting Kit 8 (CCK-8) was acquired from Dojindo Molecular Technology (Minato-ku, Tokyo, Japan). Calcein AM, propidium iodide (PI), and 4′,6-diamino-2-phenylindole (DAPI) were received from the Dingguochangsheng Biotechnology Co. Ltd. (Beijing, China). All other reagents were of at least analytical grade. HyPure water was produced by purification with a Milli-Q system (Millipore, Burlington, Vermont, USA). MDA-MB-231 and HUVEC human umbilical vein endothelial cell lines were obtained from the Chinese Academy of Sciences (Shanghai). Dulbecco's Modified Eagle Medium (DMEM), penicillin-streptomycin, fetal bovine serum (FBS), and trypsin-EDTA were bought from Gibco-BRL (Grand Island, NY, USA).

Animals and tumor model: Animals were supplied by Nanjing Pengsheng Biological Technology Co., Ltd. (Nanjing, China) and raised in the Laboratory Animal Center of Donghua University (Shanghai, China). All animal experiment operations were conducted in accordance with the Guidelines for the Care and Use of Laboratory Animals of Donghua University, and approved by the Experimental Animal Ethics Committee of Donghua University.

4.2 Construction of functional nanosheets

B NSs were prepared by coupling thermal oxidation etching and liquid exfoliation technologies. Boron powder (0.5 g) was dispersed in 100 mL of a mixture of ethanol and NMP (1:1 *v/v*), and the solution sonicated for 5 h in an ice bath before being centrifuged at 3,000 rpm for 10 min to pellet the bulk powder. Next, the supernatant was removed by centrifugation at 12,000 rpm for 20 min, and the product washed three times with ethanol. Residual solvent after washing was evaporated by vacuum rotary evaporation. The resultant B sheets were placed in a crucible and heated at 650 °C for 2 h in air. After being allowed to cool to ambient temperature, the product was collected and sonicated in water. The resulting suspension was finally centrifuged at 12,000 rpm for 30 min and the precipitate collected for future use.

B NSs (2 mg) were dispersed in distilled water (10 mL). H_2N-PEG-NH_2 (10 mg) was added to the B NSs/H_2O suspension, with sonication applied for 30 min followed by stirring at room temperature for 12 h. The resulting mixture was centrifuged at 2500 rpm and 4 °C for 30 min to remove unreacted H_2N-PEG-NH_2 molecules, and the solid product washed three times with water and dried under high vacuum (60 °C) for 24 h.

In order to prepare B-PEG-cRGD NSs, B-PEG NSs (60 mg) were dispersed in PBS (5 mL, pH = 6.5), and then EDC (3.8 mg) and NHS (2.3 mg) were added quickly to the dispersion to active the B-PEG sample. The suspension was sonicated for 15 min. Next, cRGD (9.3 mg) was separately dissolved in PBS (5 mL, pH = 6.5) and the cRGD solution added slowly to the activated B-PEG NSs. The reaction was allowed to proceed with stirring at room temperature for 24 h. The products were dialyzed against ultrapure water using a cellulose membrane (MWCO: 3500 Da) for 3 d to remove the reactant and collect B-PEG-cRGD.

B-PEG-cRGD was dispersed in PBS (pH = 7.0) followed by the addition of 10 mL of a 1 mg/mL DOX solution in PBS. The mixed solution was stirred at room temperature for 24 h in the dark. Then mixed with 17AAG at a concentration of 0.5 mg/mL and stirred at room temperature overnight to obtain DOX-17AAG@B-PEG-cRGD before being dialyzed against distilled water using a cellulose membrane (MWCO 3,500 Da) for 2 d. The amount of DOX and 17AAG loaded was quantitatively evaluated using UV–Vis spectrophotometry at λ = 480 nm and HPLC, respectively.

4.3 Materials characterization

The morphologies of the prepared nanosheets were studied by TEM on a JEM-2100UHR instrument (JEOL, Tokyo, Japan), and the thickness of B NSs were measured atomic force microscope (AFM, Agilent 5500, USA). Dynamic light scattering (DLS) and zeta potential data were obtained on a BI-200SM instrument (Brookhaven, Holtsville, NY, USA). UV−vis absorption spectra were collected from 200 to 1000 nm using a UV 3600 spectrophotometer (Shimadzu, Kyoto, Japan) at ambient temperature. X-ray photoelectron spectroscopy was carried out on an ESCALAB 250Xi instrument (Thermo Fisher, Waltham, MA, US). TGA was used to determine the thermal stability and composition of the material, with experiments performed on a TGA-101 analyzer (JB-TGA-101, Shanghai, China).

4.4 *In vitro* drug release

In vitro release of DOX and 17AAG from DOX−17AAG@B-PEG-cRGD was explored at different pH values (7.4 or 5.0), with and without NIR laser irradiation (808nm, 1 W/cm^2). The drug-loaded nanosheets (5 mg) were dispersed in PBS (2 mL) at the appropriate pH and charged into a dialysis bag (MWCO: 8–10 kDa). The dialysis bags were then placed in PBS (20 mL) at the same pH as the NS suspension and shaken at 37 °C with or without exposure to 808 nm laser irradiation (NIR laser exposure was performed for 10 min at a power density of 0.5 w/cm^2 at the beginning of the experiment). At specific time intervals, aliquots of the solution outside the dialysis bag (1 mL) were collected and replaced with an equal volume of fresh preheated buffer. The concentration of DOX was determined by UV-vis spectroscopy at 480 nm, and the 17AAG content was quantified at 254 nm using HPLC equipped with a ZORBAX SB-C18 column (Agilent, Japan). An acetonitrile/water mixture (73:27 v/v) was used as the mobile phase, with a flow rate of 1 mL/min.

4.5 Cellular uptake

MDA-MB-231 cells and HUVEC cells were separately suspended in DMEM medium augmented with penicillin-streptomycin (100 U/mL) and FBS (10% v/v) ("complete DMEM") at a concentration of 10^5 cells/mL. 1 mL of cell suspension was placed in each well of 24-well flat-bottomed culture dishes. The cells were incubated at 37 °C for 24 h under a humidified 5% CO_2 atmosphere. Subsequently, they were cultured for another 2 h with free DOX or DOX-17AAG@B-PEG-cRGD at a DOX concentration of 5 μM. After this, the medium was discarded and the cells washed twice with PBS (pH 7.4, 1 mL). Finally, the cells were fixed with aqueous glutaraldehyde solution (2.5% w/v) for 15 min at 4 °C. The cell nuclei were stained with DAPI in the dark, washed again using PBS, and images recorded with confocal laser scanning microscopy (CLSM; FV1000 microscope; Olympus, Tokyo, Japan). In addition, we performed flow cytometry analysis to further assess intracellular uptake. The treated cells were collected with free DOX or DOX-17AAG@B-PEG-cRGD, rinsed with PBS, and analyzed by flow cytometry.

4.6 *In vitro* cytotoxicity assays

Cytotoxicity was analyzed by the CCK-8 assay. Cell suspensions in complete DMEM were seeded at a density of 1×10^4 cells/well into 96-well plates (200 μL per well). The cells were incubated at 37 °C for 12 h under a humidified 5% CO_2 atmosphere. Subsequently, the medium was removed, and replaced with suspensions of the formulations (B NSs and B-PEG-cRGD) in complete DMEM. The cells were then cultured for a further 12 h, after which the CCK-8 reagent was added to each well and the plate gently shaken to aid mixing. A Multiskan FC plate reader (ThermoFisher, Shanghai, China) was used to quantify cell viability. Three independent experiments were performed, with 5 replicates in each.

4.7 Western blotting

MDA-MB-231 cells (1×10^6 cells/well) in DMEM (2 mL) were seeded in six-well plates and cultured for 24 h. The original medium was removed and suspensions of the formulations in DMEM (the concentration of 17AAG was 3 μg/mL) added. After incubation for 6 h, the medium was discarded, the cells washed twice with PBS, and 150 μL of RIPA (radio immunoprecipitation assay) reagent added to each well. The plate was shaken to ensure complete mixing of the RIPA reagent with the cells. This whole process was performed in an ice box. Afterwards, the cells were then collected by scraping. The proteins extracted from the cells were separated by SDS-PAGE (polyacrylamide gel electrophoresis), and transferred to an activated PVDF membrane. The membrane was transferred to blocking solution (5% skimmed milk) at ambient temperature and blocked for 1 h, then the primary antibody was added and the membrane incubated overnight at 4 °C. The membrane was next incubated with secondary antibodies for 30 min and washed three times. The blots for specific proteins were obtained by ECL (enhanced chemiluminescence) gel imaging system (AlphaImager Mini, ProteinSimple, San Jose, CA, USA) and analyzed by the Alpha software processing system. As a control, the expression of glyceraldehyde-3-phosphate dehydrogenase (GAPDH) was evaluated.

4.8 *In vitro* low-temperature photothermal therapy/chemotherapy

MDA-MB-231 cells were cultured in 96-well plates (1×10^4 cells/well in 200 μL complete DMEM) for 24 h. The original medium was then discarded and replaced with fresh medium containing the test materials. The cells were treated under conditions of hyperthermia (43 °C) for a certain period of time, and then transferred to physiological temperature (37 °C). The total incubation period was 20 h, after which cell viability was determined with the CCK-8 assay.

In a second series of experiments, MDA-MB-231 cells were seeded in a 96-well plate and co-cultured with 200 μL of medium containing 17AAG or 17AAG-loaded samples at a range of concentrations. The cells in NIR groups were exposed to laser irradiation for 10 min (808 nm, 1.0 W/cm^2) at the start of the experiment. After 12 h of incubation, cell viability was quantified with the CCK-8 assay.

For live/dead staining, MDA-MB-231 cells were cultured for 24 h in a six-well plate (1× 10^5 cells/well in 2.0 mL of complete DMEM). The medium was removed, replaced with complete DMEM containing the various formulations (17AAG concentration of 3μg/mL), and culture continued for 10 h with or without an initial laser irradiation period of 10 min (808 nm, 1.0 W/cm^2). Experimental groups were as follows. (I) PBS (control); (II) B-PEG-cRGD+NIR; (III) free DOX; (IV) DOX-17AAG@B-PEG; (V) DOX@B-PEG-cRGD+NIR; (VI) DOX-17AAG@B-PEG-cRGD+NIR.

The cells were washed and Calcein AM (2 μM) and PI (8 μM) added. After staining for 15 min in the dark, images (apoptotic cells, red; living cells, green) were recorded using a TE-2000U inverted phase contrast microscope (Olympus, Tokyo, Japan).

4.9 *In vivo* biodistribution

In order to evaluate the in vivo biodistribution of DOX-17AAG@B-PEG-cRGD, MDA-MB-231 cells (3×10^6 cells/mouse) were injected into the dorsum to get MDA-MB-231 tumor-bearing mice model. Healthy mice were injected with DOX@B-PEG-cRGD and DOX-17AAG@B-PEG-cRGD at the equal DOX dose (5 mg DOX/kg) by tail intravenous injection. At 8 h post injection, the mice were sacrificed,

and the main organs (heart, liver, spleen, lung, and kidney) and tumors were dissected and weighed. The selected tissue is then digested, diluted, and filtered. Finally, the content of B in the solution was measured by ICP-OES (Prodigy-ICP, LEEMAN LABS INC., USA). In addition, collect feces and urine at different time points (4, 8, 12, 24, 36 h) and determine the content of B by ICP-OES spectroscopic analysis to study the metabolism of DOX-17AAG@B-PEG-cRGD in vivo.

4.10 *In vivo* anti-cancer effects

To establish the breast tumor model, MDA-MB-231 cells (3×10^6 cells/mouse) were injected into the dorsum, and tumor nodules periodically examined with calipers. Tumor-bearing nude mice with tumor volumes of ca. 100 mm^3 were randomly divided into six groups (n = 5), and injected intravenously into the tail vein with the formulation under test. The following treatments were investigated: PBS+NIR, B-PEG-cRGD with NIR irradiation, free DOX, free 17AAG, DOX-17AAG@B-PEG, DOX@B-PEG-cRGD with NIR irradiation, and DOX-17AAG@B-PEG-cRGD with NIR irradiation. The amount of DOX in each treatment was set at 5 mg/kg. In the groups subject to NIR treatment, an 808 nm laser with a power density of 0.5 W/cm^2 was applied to the animals for 15 min every other day. During the experiment, the length and width of the tumors were measured every two days to calculate the volume ($length\times width^2/2$) and the body weight data recorded.

4.11 Histological Analysis

The tumor tissues and major organs (heart, lung, spleen, liver, and kidney) were excised from the mice after the 14 day treatment period, and fixed in 4% aqueous formaldehyde. They were then embedded in paraffin and sliced into 5 μm sections. These sections were stained with hematoxylin and eosin (H&E) and studied under an optical microscopic. In addition, TUNEL (TdT-mediated dUTP-biotin nick end labeling) staining was used to analyze apoptosis.

4.12 Statistical Analysis

The data for all experiments are reported as mean ± SD, and each experiment was carried out at least in triplicate. Statistical significance was examined using the Student's t-test, and * indicates a significant difference ($P< 0.05$).

Conflicts of interest

The authors declare no competing financial interest.

Acknowledgement

This investigation was supported by grant 16410723700 from the Science and Technology Commission of Shanghai Municipality, the Biomedical Textile Materials "111 Project" of the Ministry of Education of China (No. B07024), and the UK-China Joint Laboratory for Therapeutic Textiles (based at Donghua University).

References

1. R. L. Siegel, K. D. Miller and A. Jema, *CA: a cancer journal for clinicians*, 2016, **66**, 7-30.
2. C. Ju, R. Mo, J. Xue, L. Zhang, Z. Zhao, L. Xue, Q. Ping and C. Zhang, Angew. Chem. Int. Ed.,2014, **53**, 6253−6258.
3. P. Song, S. Kuang, N. Panwar, G. Yang, D. J. H. Tng, S. C. Tjin, W. J. Ng, M. B. A. Majid, G. Zhu and K.-T. Yong, Adv. Mater., 2017, **29**, 1605668.
4. Z. Luo, X. Ding, Y. Hu, S. Wu, Y. Xiang, Y. Zeng, B. Zhang, H. Yan, H.Zhang and L. Zhu, ACS Nano, 2013, **7**, 10271−10284.
5. A. Bansal and Y. Zhang, Acc. Chem. Res., 2014, **47**, 3052− 3060.
6. Y. Sun, C. Kang and F. Liu, Drug Development Res., 2017, **78**, 283-291.
7. J. R. Wu, G. R. Williams, S. W. Niu, F. Gao, R. R. Tang and L. M. Zhu, Adv. Sci., 2019, **6**, 1802001.
8. J. R. Wu, D. H. Bremner, S. W. Niu, H. L. Wu, J. Z. Wu, H. J. Wang, H. Y. Li and L.M. Zhu, Chem. Eng. J., 2018, **342**, 90-102.
9. D. Chimene, D. L. Alge and A. K. Gaharwar, Adv. Mater., 2015, **27**, 7261.
10. Y. Chen, Y. Wu, B. Sun, S. Liu and H. Liu, Small, 2017, **13**, 1603446.
11. B. Yang, Y. Chen and J. Shi, Chem, 2018, **4**, 1284-1313.
12. V. Shanmugam, S. Selvakumar and C. S. Yeh, Chem. Soc. Rev., 2014, **43**, 6254.
13. X. Zhu, X. Ji, N. Kong, Y. Chen, M. Mahmoudi, X. Xu and T. Gan, ACS Nano, 2018, **12**, 2922.
14. H. Lin, S. Gao, C. Dai, Y. Chen and J. Shi, J. Am. Chem. Soc., 2017, **139**, 16235-16247.
15. Y. Zhu, S. Murali, W. Cai, X. Li, J. W. Suk, J. R. Potts and R. S. Ruff, Adv. Mater., 2010, **22**, 3906-3924.
16. X. Zeng, M. Luo, G. Liu, X. Wang, W. Tao, Y. Lin and L. Mei, Adv. Sci., 2018, **5**, 1800510.
17. W. Tao, X. B. Zhu, X. H. Yu, X. W. Zeng, Q. L. Xiao, X. D. Zhang, X. Y. Ji, X. S. Wang, J. J. Shi, H. Zhang and L. Mei, Adv. Mater., 2017, **29**, 1603276.
18. B. Albert and H. Hillebrecht, Angew. Chem. Int. Ed., 2009, **48**, 8640.
19. T. Ogitsu, E. Schwegler and G. Galli, Chem. Rev., 2013, **113**, 3425-3449.
20. X. J. Wang, J. F. Tian, T. Z. Yang, L. H. Bao, C. Hui, F. Liu and H. J. Gao, Adv. Mater., 2007, **19**, 4480-4485.
21. X. Y. Ji, K. Na, J. Q. Wang, W. L. Li, Y. L. Xiao, S. T. Gan, Y. Zhang, Y. J. Li, X. R. Song, Q. Q. Xiong, S. J. Shi, Z. J. Li, W. Tao, H. Zhang, L. Mei and J. J. Shi, Adv. Mater., 2018, **30**, 1803031.
22. N. Bertrand, J. Wu, X. Xu, N. Kamaly and O. C. Farokhzad, Adv. Drug Deliver Rev., 2014, **66**, 2-25.
23. A. E. Nel, L. Mädler, D. Velegol, T. Xia, E. M. Hoek, P. Somasundaran and M. Thompson, Nat. Mater., 2009, **8**, 543-557.
24. R. Zeineldin, M. Al-Haik and L. G. Hudson, Nano Lett., 2009, **9**, 751-757.
25. M. Hamidi, A. Azadi and P. Rafiei, Drug Deliv., 2006, **13**, 399−409.
26. Q. He, Z. Zhang, F. Gao, Y. Li and J. Shi, Small, 2007, **7**, 271−280.
27. F. Danhier, A. Le Breton and V. Préat, Mol. Pharmaceut., 2012, **9**, 2961-2973.
28. D. B. Pike and H. Ghandehari, Adv. Drug Deliver Rev., 2010, **62**, 167-183.
29. X. Huang, P. K. Jain, I. H. El-Sayed and M.A. El-Sayed, Laser. Med. Sci., 2008, **23**, 217.
30. J. Shao, H. Xie, H. Huang, Z. Li, Z. Sun, Y. Xu and H. Wang, Nat. Commun., 2016, **7**, 12967.
31. W. H. Chen, G. F. Luo, Q. Lei, S. Hong, W. X. Qiu, L. H. Liu and X. Z. Zhang, ACS Nano, 2017, **11**, 1419-1431.
32. D. Yoo, H. Jeong, S. H. Noh, J. H. Lee and J. Cheon, Angew. Chem. Int. Ed., 2013, **52**, 13047-13051.
33. S. W. Lee, J. W. Lee, J. H. Chung and J. K. Jo, The World Journal of Men's Health, 2013, **31**, 247-253.

34. Y. Cao, X. Meng, D. Wang, K. Zhang, W. Dai, H. Dong and X. Zhang, ACS Appl. Mater. Inter., 2018, **10**, 17732-17741.
35. G. C. Li, N. F. Mivechi and G. Weitzel, Int. J. Hyperther., 1995, **11**, 459-488.
36. J. R. Wu, D. H. Bremner, S. W. Niu, M. H. Shi, H. J. Wang, R. R. Tang and L. M. Zhu, ACS Appl. Mater. Inter., 2018, **10**, 42115 - 42126.
37. K. Zhang, X. Meng, Y. Cao, Z. Yang, H. Dong, Y. Zhang and X. Zhang, Adv. Funct. Mater., 2018, **28**, 1804634.
38. Y. Yang, W. Zhu, Z. Dong, Y. Chao, L. Xu, M. Chen and Z. Liu, Adv. Mater., 2017, **29**, 1703588.
39. H. H. Luo, Q. L. Wang, Y. B. Deng, T. Yang, H. T. Ke, H. Yang, H. He, Z. Q. Guo, D. Yu, H. Wu and H. B.Chen, Adv. Funct. Mater., 2017, **27**, 1702834
40. W. Yan, J. Xiao, T. Liu, W. Huang, X. Yang, Z. Wu and M. Qian, Tumor Biol., 2013, **34**, 1391-1397.
41. N. Zaarur, V. L. Gabai, J. A. Porco, S. Calderwood and M. Y. Sherman, Cancer Res., 2006, **66**, 1783-1791.
42. Y. W. Chen, Y. L. Su, S. H. Hu and S. Y. Chen, Adv. Drug Deliver Rev., 2016, **105**, 190-204.
43. Z. Xie, D. Wang, T. Fan, C. Xing, Z. Li, W. Tao and H. Zhang, J. of Mater. Chem. B, 2018, **6**, 4747-4755.
44. S. Mura, J. Nicolas and P. Couvreur, Nat. Mater., 2013, **12**, 991-1003.
45. S. Takayama, S. Ishii, T. Ikeda, S. Masamura, M. Doi and M. Kitajima, Anticancer Res., 2005, **25**, 79-83.
46. C. Lv, H. W. Zeng, J. X. Wang, X. Yuan, C. Zhang, T. Fang, P. M. Yang, T. Wu, Y. D. Zhou, D. G. Nagle and W. D. Zhang, Cell Death Dis., 2018, **9**, 165.
47. Y. W. Won, S. M. Yoon, C. H. Sonn, K. M. Lee and Y. H. Kim, ACS Nano, 2011, 5, 3839−3848.

